TRENDS IN SCIENCES 2025; 22(9): 10377
https://doi.org/10.48048/tis.2025.10377
RESEARCH ARTICLE

Enhancing Supercapacitor Performance with Multilayered Tungsten (VI) Oxide Nanoparticles/Reduced Graphene Oxide and Activated Carbon

Santi Rattanaveeranon[1,*] and Knavoot Jiamwattanapong[2]

[1]Applied Physics Material Laboratory (APM Lab.), Physics Program, Faculty of Liberal Arts, Faculty of Science and Technology, Rajamangala University of Technology Rattanakosin, Nakhon Pathom 73170, Thailand
[2]Department of General Education-Mathematics, Faculty of Liberal Arts, Rajamangala University of Technology Rattanakosin, Nakhon Pathom 73170, Thailand

([*]Corresponding author's e-mail: santi.r@rmutr.ac.th)

Received: 16 April 2025, Revised: 10 May 2025, Accepted: 17 May 202, Published: 10 July 2025

Abstract

Developing hybrid graphene-metal oxide materials is crucial for advancing high-performance supercapacitor electrodes due to their unique pseudocapacitive properties and scalability. This study presents a cost-effective approach to fabricating multilayer supercapacitor electrodes by integrating tungsten (VI) oxide (WO_3) nanoparticles with reduced graphene oxide (rGO) sheets (18.20 ± 0.12 µm). WO_3 nanoparticles (21.56 ± 1.83 nm) were deposited onto rGO sheets to enhance pseudocapacitive behavior, forming a WO_3/rGO nanocomposite. Additionally, activated carbon (6.36 ± 0.32 µm) derived from durian peels and carbon from durian peel ash were incorporated as composite layers, providing a sustainable alternative for electrode fabrication. A screen-printed electrode with an approximately 500 µm-thick WO_3/rGO layer achieved an impressive specific capacitance of 733.30 $F \cdot g^{-1}$ at a current density of 1 $A \cdot g^{-1}$ and exhibited excellent cyclic stability, retaining 95 % of its capacitance after 5,000 charge-discharge cycles. This innovative approach offers a sustainable and efficient strategy for enhancing supercapacitor performance, with promising implications for enhancing energy storage capacity in next-generation technologies.

Keywords: Hybrid graphene-metal oxide materials, Tungsten Oxide (WO_3), Reduced Graphene Oxide (rGO), Activated carbon, Supercapacitor performance

Introduction

Among various carbon nanomaterials, such as amorphous carbon, graphite, carbon nanotubes (CNTs), nanodiamonds, and graphene, graphene has garnered significant attention in both research and industry due to its promising scientific applications [1]. Graphene, often referred to as a "wonder material", is a two-dimensional (2D) material composed of sp^2-hybridized carbon atoms arranged in a single layer of hexagonal rings [2]. It exhibits outstanding properties, including high electrical and thermal conductivity, a large specific surface area, excellent carrier mobility, high chemical stability, superior optical transmittance, and exceptional mechanical strength [3]. These remarkable properties make graphene suitable for diverse applications, such as supercapacitors, sensors, photonic devices, transparent conductive electrodes, nanoelectronics, and photocatalysis [4].

Graphene is commonly produced via chemical reactions starting from graphite. This process typically involves the oxidation of graphite powder to graphite oxide, followed by the conversion of graphite oxide to graphene oxide (GO), and its subsequent reduction to reduced graphene oxide (rGO) [5]. rGO has a structure similar to pure graphene [6]. GO is often prepared using the Hummers method, which introduces a large number of oxygen-containing functional groups (e.g., -COOH, -OH, C = O, and -CHO) on the surface and edges of the graphene sheets. These functional groups impede

electron movement in GO; thus, reducing them enhances electrical conductivity and improves the material's electronic properties [7].

Various reduction methods, such as chemical reduction [8], thermal reduction [9], microwave-assisted reduction [10], photoactive reduction [11], and hydrothermal reduction [12], have been developed to transform GO into rGO. The resulting rGO serves as a foundation for the production of graphene-metal oxide nanocomposites, which exhibit significantly improved properties compared to pristine rGO. The wrinkled structure of rGO acts as a supporting matrix for the growth of nanoscale metal oxide crystals. Furthermore, integrating metal oxides with graphene introduces new functionalities and enhances the physical, chemical, and mechanical properties of the composite materials [13]. Different metal oxide-graphene composites, including TiO_2 [14], Mn_3O_4 [15], ZnO [16], CdO [17], MoO_3 [18], CeO_2 [19], NiO [20], Co_3O_4 [21], and MgO [22], have been extensively studied for their unique properties and applications. Among these, tungsten oxide (WO_3) integrated with rGO has gained significant attention due to its excellent optical and electrochemical properties.

The integration of graphene with metal oxides, such as tungsten oxide (WO_3), has demonstrated significant improvements in electrochemical performance. However, to be viable for large-scale applications in energy storage devices, these materials must be further optimized. WO_3 is a non-toxic transition metal oxide and an n-type semiconductor with a narrow bandgap of 2.4 - 2.8 eV, making it highly suitable for visible light applications [23]. It also possesses a high intrinsic carrier density, mechanical stability, and chemical resistance, enabling its use in sensors, electrochromic devices, photocatalysis, batteries, optoelectronics, dye-sensitized solar cells, and supercapacitors [24]. However, the primary limitations of WO_3 are its low energy density and electrical conductivity. To overcome these challenges, rGO sheets are employed to enhance the electrical conductivity and overall performance of WO_3 composites. The 2D structure of rGO facilitates the growth of WO_3 nanoparticles, significantly improving the composite's electrical properties. The synthesis of WO_3-rGO composites has been extensively studied, and various synthetic approaches, including hydrothermal [25], precipitation [26], and oxidation of WS_2 nanoparticles at room temperature [27], have been reported. Researchers have demonstrated that WO_3 nanofibers coated on rGO surfaces exhibit enhanced electrochemical properties [28]. Similarly, WO_3 nanoflowers grown on graphene nanosheets have shown excellent performance as electrode materials for supercapacitors. This research not only aims to enhance the electrical capacity and efficiency of energy storage systems but also seeks to address broader issues related to energy accessibility. By incorperating activated carbon derived from durian peel as a low-cost and sustainable material, the study offers a potential solution for the development of high-performance supercapacitors that are accessible to communities with limited resources. Through this approach, the work aspires to deliver practical benefits and improve quality of life, ensuring that advances in material science lead to real-world impact rather than remaining confined to academic publication.

In this project, a hybrid WO_3/rGO electrode was developed to fabricate a supercapacitor with enhanced electrical capacity and faster charging capability. Additionally, an activated carbon (AC) layer prepared from durian peel was incorporated as a carrier layer in the final step to optimize the electrode's performance further.

Materials and methods

Materials

Graphite powder (99.99 % purity; Lianyungang Jinli Carbon), sodium nitrate ($NaNO_3$), potassium permanganate ($KMnO_4$), sulfuric acid (H_2SO_4, 97 wt%), hydrogen peroxide (H_2O_2, 30 wt%), hydrazine monohydrate ($NH_2NH_2{\cdot}H_2O$), sodium hydroxide (NaOH), Nafion-117, tungsten (VI) chloride (WCl_6) and distilled water were used in this study. All chemicals were of analytical grade and used without further purification.

Graphene oxide synthesis

Graphene oxide (GO) was synthesized from graphite using the Hummers method. In this process, 3 g of graphite powder were mixed with 69 mL of sulfuric acid (H_2SO_4), 1.5 g of sodium nitrate ($NaNO_3$), and 9 g of potassium permanganate ($KMnO_4$) in a container maintained at a temperature below 20 °C. The mixture was stirred for 30 min while ensuring the temperature did not exceed 35 °C.

Next, 138 mL of deionized water was slowly added to the mixture, as the reaction is highly exothermic. The temperature was then adjusted to 80 °C, and the mixture was stirred for an additional 30 min. The resulting mixture turned brown. The container was placed in a cold water bath for 10 s before 3 mL of 30 % v/v hydrogen peroxide (H_2O_2) was added. At this stage, the graphene oxide separated as a light-yellow solution, while manganese dioxide (MnO_2) formed as a brown precipitate at the bottom of the beaker.

The beaker was left overnight to ensure the reaction was completed. The graphene oxide solution (yellow solution) was carefully aspirated using a pipette and filtered under vacuum. The resulting material was washed multiple times with deionized water until the washing water reached a neutral pH of approximately 7. It was then washed sequentially with methanol and acetone. Finally, the material was vacuum-dried for 3 h to obtain graphene oxide [29].

Reduced graphene oxide synthesis

To synthesize reduced graphene oxide (rGO), 0.5 g of graphene oxide powder was dissolved in 250 mL of deionized water. The solution was subjected to ultrasonication at 40 kHz for 20 min to ensure proper dispersion.

Hydrazine monohydrate solution ($NH_2NH_2{\cdot}H_2O$) was then added to the mixture in a ratio of GO: $NH_2NH_2{\cdot}H_2O$ = 3 g:1 % v/v. The reaction was carried out using the reflux method at 90 °C for 12 h.

The resulting product was filtered using a vacuum filtration system with filter paper (Whatman No. 40). The sample was washed several times with deionized water until the filtrate reached a neutral pH of approximately 7. Finally, the sample was sequentially washed with methanol and acetone before drying [30].

Tungsten oxide nanoparticles synthesis

Dissolve 1 g of tungsten chloride in 50 mL of deionized water in a 250-mL glass bottle. Microwave the solution at 400 W for 30 s, pausing for 10 s after each interval, for a total of 5 min. Allow the solution to cool to room temperature. Ultrasonicate at 40 kHz for 20 min, then filter the WO_3 precipitate using a vacuum filter. Collect the white precipitate, which represents pure WO_3, after natural cooling of the autoclave [31].

Tungsten oxide/reduced graphene oxide nanoparticles synthesis

Dissolve 0.5 g of graphene oxide in 50 mL of deionized water and add 200 mg of tungsten chloride powder. Transfer the mixture to a 250-mL glass bottle and microwave at 400 W for 30 s, pausing for 10 s after each interval, for a total of 5 min. Allow the solution to cool to room temperature, ultrasonicate at 40 kHz for 20 min, and filter the WO_3/rGO composite precipitate using a vacuum filter. The resulting composite material has a color ranging from grey to black [32].

Preparation of activated carbon (AC) powder from durian peels

Durian peels were thoroughly washed with filtered water (twice) and rinsed with deionized water. The peels were cut into pieces measuring 2 × 1 cm and burned in a muffle furnace at 650 °C for 2 h under an Ar atmosphere. The resulting material was ground and dried in a 50-mL Teflon bottle using a stainless steel ball mill for 12 h. The reaction involved 6 stages using concentrated sulfuric acid, followed by filtration and washing with filtered and deionized water. Finally, the material was dried, burned in a muffle furnace at 650 °C for 2 h under an Ar atmosphere, and sieved through a steel wire mesh [30].

Characterizations

The composite materials—GO, rGO, AC, and WO_3/rGO—were deposited onto glass slides and dried using a hotplate prior to characterization. Surface morphology was examined using field-emission scanning electron microscope (FESEM; Hitachi, S-4700 model). Raman spectroscopy (InVia, Renishaw) was employed to identify the graphitic structure, using a laser excitation wavelength of 514 nm. The structural properties of the composites were analyzed via X-ray diffraction (XRD) using a Bruker D8 Advance diffractometer with Cu K_α radiation, operated at a low scanning speed of 0.021° s^{-1}.

Fourier-transform infrared spectroscopy (FTIR; Thermo) was conducted to identify functional groups. Samples were prepared by mixing composite powders with 0.02 g of potassium bromide (KBr), then scanning over a wavenumber range of 4,000 - 1,000 cm^{-1}. Thermogravimetric analysis (TGA) was performed

from room temperature to 1,000 °C at a heating rate of 5 °C/min.

The specific surface area (SSA) of the samples was measured using the Brunauer-Emmett-Teller (BET) method based on nitrogen adsorption-desorption isotherms. BET analysis was conducted with a Microceritics volymetric adsorption system at 77 K, over a relative pressure range of $0 \leq P/P_o \leq 0.99$. While commonly applied, the BET method may overestimate SSA in microporous materials due to gas condensation phenomena. In graphene-based materials, the formation of multilayer stacks can also limit the accessible surface area. These factors were considered when interpreting the results. While commonly applied, the BET method may overestimate SSA in microporous materials due to gas condensation phenomena. In graphene-based materials, the formation of multilayer stacks can also limit the accessible surface area. These factors were considered when interpreting the results.

Preparation of thin films on three-electrode systems

Samples of GO, WO_3 NPs, AC, WO_3/rGO/AC, and rGO were finely ground in an agate mortar. A 0.1 mg/mL Nafion-117 solution in ethanol was prepared, and the samples were coated onto three-electrode systems (screen-printed electrodes, SPEs) and allowed to dry. A 2 M KOH solution was applied to the electrodes to measure their electrochemical properties [33].

Electrochemical measurements

Electrochemical behavior studies were conducted using a screen-printed electrode system consisting of a platinum working electrode, a platinum counter electrode, and an Ag/AgCl reference electrode. Cyclic voltammetry (CV) and charge/discharge techniques were employed to evaluate the electrical behavior within a potential range of 0 to 0.5 V. The electrochemical performance of various samples, including GO, rGO, WO_3, WO_3/rGO, AC, and WO_3/rGO/AC, was compared. The results were analyzed and interpreted accordingly.

Results and discussion

TGA study

Figure 1 presents the thermogravimetric analysis (TGA) cuvres used to evaluate the thermal stability of the samples. The TGA curve of GO exhibits three distinct weight-loss stages: ~16 % at 100 °C due to the evaporation of adsorbed water; ~43% at 240 °C attributed to the decomposition of oxygen-containing functional groups; and ~69% at 510 °C corresponding to the combustion of carbon framework [34]. Above 510 °C, the weight remained nearly constant, indicating the complete decomposition of GO.

In contrast, the WO_3/rGO composite showed a total weight loss of ~9.83% within the 30 - 800 °C temperature range, with minor decomposition leading to an overall weight loss of ~17%. Below 230 °C, the observed weight loss was primarily due to the pyrolysis of residual oxygen functional groups attached to the 2D graphite structure [35]. Between 300 and 600 °C, further weight loss occurred as a result of the oxidative degradation of the carbon lattice [36]. Based on the residual mass, the WO_3 content on the rGO surface was estimated to be 17 wt%.

Raman study

As shown in **Figure 2**, the Raman spectra of pure WO_3 and WO_3/rGO nanocomposites, tested in the range of 500 - 3500 cm^{-1}, exhibit four sharp and well-defined bending vibration bands in the W-O-W bonds at ~272 cm^{-1} and ~326 cm^{-1}. The sharp peak at ~272 cm^{-1} is attributed to the bending vibration mode of W^{4+}-O bonds, while ~326 cm^{-1} corresponds to the bending vibration mode of W^{5+}-O bonds [37]. Additionally, the graphitic peaks at ~717 cm^{-1} and ~807 cm^{-1} are associated with the elastic vibration of the O-W-O stretching mode in WO_3 [38].

For the WO_3/rGO nanocomposites, the stretching mode and vibration pattern were observed to shift slightly, likely due to strong interactions between WO_3 and the rGO surface. Furthermore, the (d) and (g) bands of GO in the nanocomposites also shifted slightly, potentially caused by crystal lattice vibrations and the introduction of functional groups in the carbon network [39]. This shift indicates charge transfer between the rGO and WO_3 sheets, resulting in crosslinking between the two.

The I_D/I_G ratio for the WO_3/rGO nanocomposites was found to be 0.75, indicating the presence of defects in the rGO crystal lattice. A significant increase in the I_D/I_G ratio was observed, from 0.10 for GH to 0.60 for GO, indicating defect formation in rGO and WO_3/rGO sheets. This increase is attributed to the nucleation of WO_3 on the GO layer, forming a strong interface via C-O-W bonds [37]. These results demonstrate the efficient reduction of GO during the synthesis of WO_3/rGO nanocomposites.

X-ray study

Figure 3 shows the X-ray diffraction (XRD) patterns of (a) WO_3/rGO nanocomposites and (b) pure WO_3 nanoparticles, recorded in the 2θ range of 10° - 80°. The XRD pattern of the WO_3 nanoparticles (NPs) revealed a pure monoclinic phase with no observable impurity peaks. The diffraction peaks were indexed to the monoclinic crystal planes at (002), (020), (211), (022), (122), (114), (420), and (242), consistent with the JCPDS card No. 83-0950 [38], confirming high crystallinity and phase purity. The most intense peaks corresponded to the (200), (020), and (002) planes.

In the case of WO_3/rGO nanocomposites, the XRD patterns showed reduced intensity of WO_3 peaks and slight shifts in peak positions with increasing rGO content. These changes indicate interactions between WO_3 nanoparticles and functional groups present on the rGO surface [39]. Notably, a characteristic peak of reduced graphene oxide (rGO) appeared at $2\theta \approx 25.5°$, corresponding to the (002) plane, suggesting successful reduction of GO and suppression of restacking due to interlayer spacing effects.

FTIR study

FTIR analysis was conducted to investigate the chemical composition and interaction between WO_3 and GO. The FTIR spectra showed prominent broad absorption peaks around 3,400 cm^{-1}, corresponding to the stretching vibration of hydroxyl groups (-OH) and absorbed water [40]. In GO, the characteristic peak at 1,675 cm^{-1} represents C = O stretching, while the peak at 1,623 cm^{-1} corresponds to hydroxyl groups (O-H) from intercalated water [41].

In the WO_3 sample, the peaks below 1,000 cm^{-1} correspond to W = O and O-W-O stretching vibrations [42]. In the WO_3/rGO nanocomposites, the peak at 1,571 cm^{-1} is attributed to the COO^- stretching vibration, indicating interactions between carboxyl groups on the graphene surface and WO_3 [43]. A peak at 1,400 cm^{-1} corresponds to C-O functional groups. In contrast, the GO sample exhibits an absorption peak at 1,631 cm^{-1}, which is associated with the bending vibration mode of O-H groups [34]. These FTIR results confirm the successful interaction between WO_3 and rGO during the synthesis process.

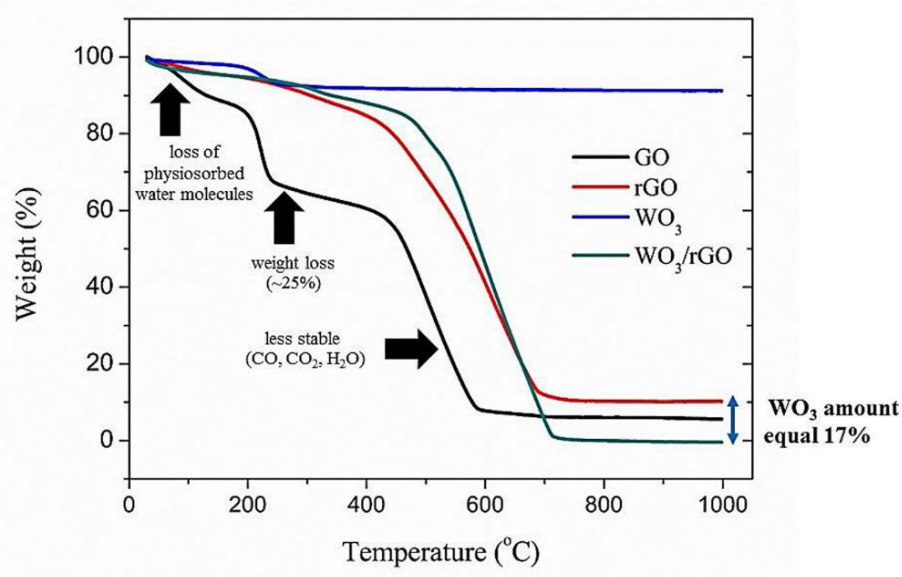

Figure 1 TGA curves of GO, rGO, WO_3, and WO_3/rGO samples.

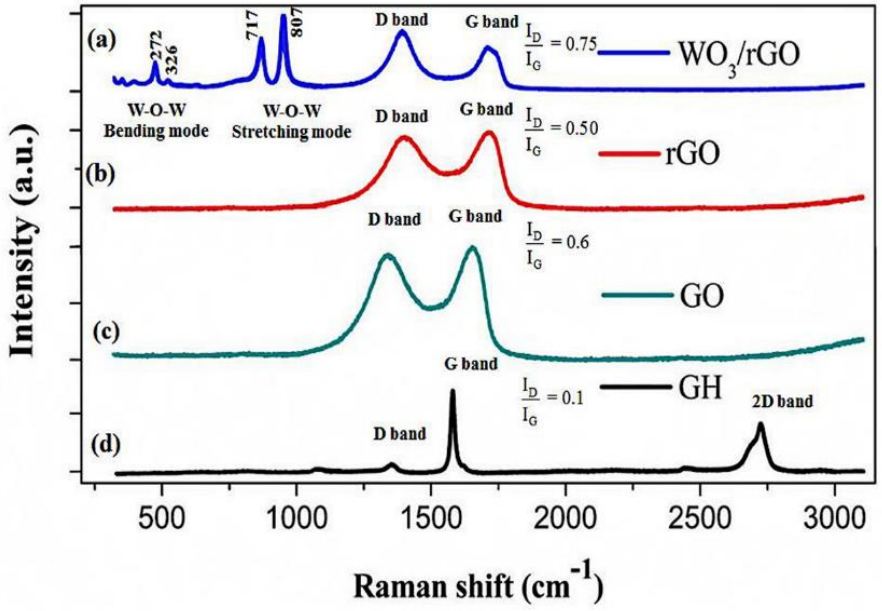

Figure 2 Raman Spectra of (a) WO_3/rGO, (b) rGO, (c) GO, and (d) GH powder.

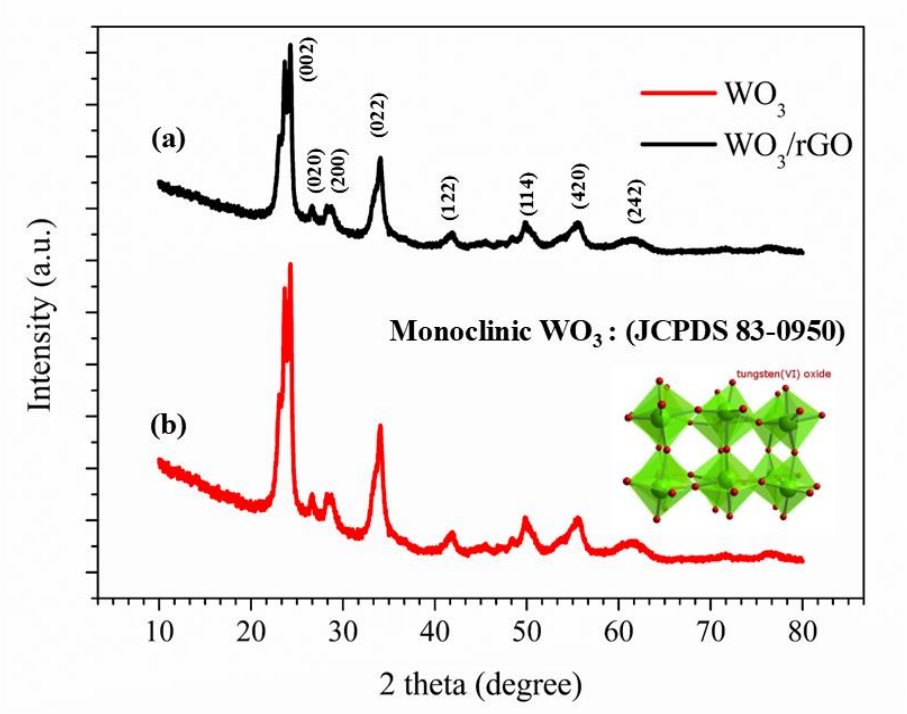

Figure 3 XRD patterns of (a) WO_3/rGO nanocomposites and (b) WO_3 nanoparticles.

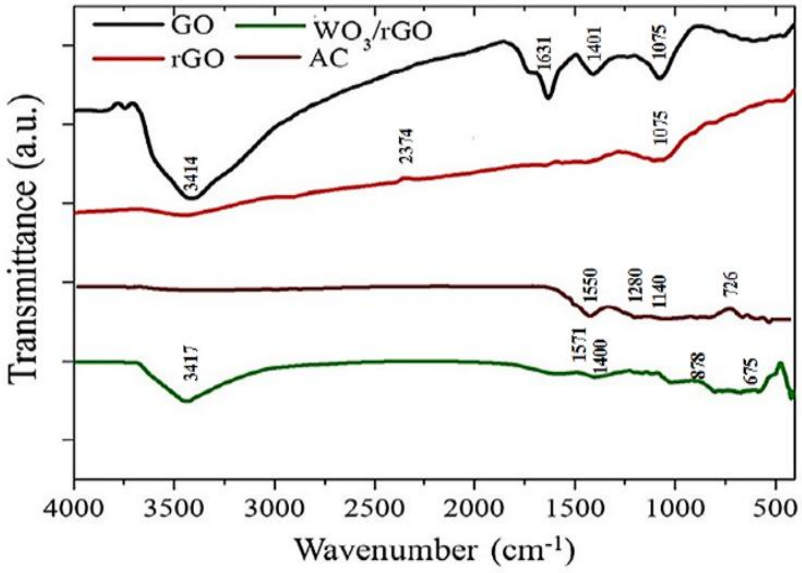

Figure 4 FTIR spectra of GO, rGO, AC, and WO_3/rGO nanocomposites.

Morphological analysis

FESEM study

Field-emission scanning electron microscopy (FESEM) was used to study the morphology and surface texture of the synthesized samples. The FESEM images of GO revealed layered structures with visible folds and wrinkles, typical of its two-dimensional morphology. The wrinkled surface provided a large specific surface area, enabling the attachment of WO_3 nanoparticles.

The WO_3 nanoparticles exhibited a flower-like morphology, with an average diameter of 21.56 ± 0.0834 nm, as calculated using the ImageJ software. In the WO_3/rGO nanocomposites, WO_3 nanoparticles were uniformly distributed on the rGO surface. Elemental analysis using energy-dispersive X-ray spectroscopy (EDS) confirmed the presence of W, O, and C, further verifying the formation of WO_3/rGO nanocomposites.

After synthesizing and characterizing the nanocomposites, the electrochemical performance of the supercapacitor was evaluated using a 3-electrode setup. The results revealed that supercapacitors incorporating WO_3 as a dopant in a high concentration of KOH have been reported, but many researchers suggest that these supercapacitors are only suitable for certain electrolyte solutions [42]. In contrast, pure reduced graphene oxide (rGO) supercapacitors may exhibit relatively low specific capacitance values, even though these values are theoretically promising. The rGO layers may undergo agglomeration and stacking, which can lead to low capacitance due to reduced interaction between the rGO electrode and the electrolyte [44]. The specific characteristics of activated carbon derived from durian peel, used in this study, were investigated in a previously published journal article [32].

Electrochemical analyses

The integration of electric double-layer capacitance (EDLC) properties from activated carbon (AC) with the pseudocapacitive characteristics of WO_3/rGO enhances both the specific capacitance and overall electrochemical performance of the resulting supercapacitor. This combination addresses the limitations of low-efficiency materials in energy storage applications and contributes to improving system efficiency. Such advancements have the potential to broaden the application of high-performance capacitors in energy storage systems, particularly in high-efficiency electrical infrastructure.

This study focuses on the use of activated carbon (AC) as a conductive carrier layer, leveraging its high specific surface area and excellent electrical conductivity to enhance supercapacitor performance. Five different electrodes were tested: GO, rGO, WO_3, WO_3/rGO, and AC: WO_3/rGO, with Nafion-117 used as a binder to ensure firm adhesion of the active materials to the electrode surface. The charge storage behavior was analyzed using voltammetry [45].

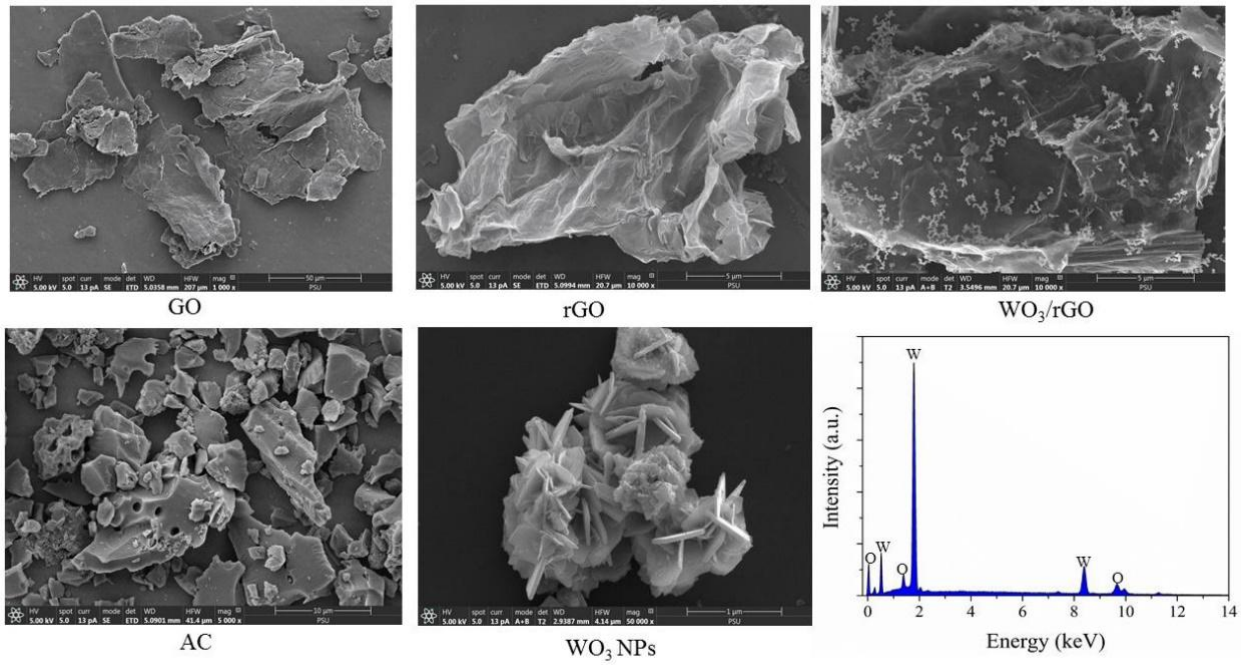

Figure 5 FESEM images of GO, rGO, WO_3/rGO nanocomposites, AC, WO_3 NPs, and EDS spectra.

Figures 6(a) and **6(b)** present the cyclic voltammetry (CV) results, which show nearly rectangular shapes for all electrodes—characteristic of ideal capacitive behavior—and are compared against the performance of the pure rGO electrode. Among the tested materials, the WO_3/rGO composite exhibited the highest capacitance, indicating a significant contribution from the pseudocapacitive mechanism. The area under the CV curve for the WO_3/rGO electrode was substantially larger than that of the other samples, confirming enhanced specific capacitance and strong electrochemical interactions between rGO and WO_3. The calculated results align with the cyclic voltammetry (CV) data, indicating a low capacitance of 117.22 $F \cdot g^{-1}$ for the rGO electrode, a high specific capacitance of 697.29 $F \cdot g^{-1}$ for the WO_3/rGO nanocomposite, and a maximum capacitance of 733.30 $F \cdot g^{-1}$ for the WO_3/rGO/AC electrode. The AC electrode has a specific capacitance of 137.25 $F \cdot g^{-1}$, which acts as a carrier for the electrons, facilitating better movement of electrons in the WO_3/rGO electrode. Therefore, an increase of 36.01 $F \cdot g^{-1}$ was observed when comparing the WO_3/rGO/AC nanocomposite, and an increase of 616.08 $F \cdot g^{-1}$ when comparing the WO_3/rGO/AC electrode with the rGO electrode. This suggests an improvement in supercapacitor performance by combining the properties of EDLC supercapacitors with those of pseudocapacitive materials.

Figure 6(b) also illustrates the effect of scan rate on charge storage performance. The scan rate, in this context, refers to the rate of voltage change over time, which directly influences the current response. The specific capacitance (C_{sp}) can be calculated using the formula $C_{sp} = I \cdot \Delta t / m \cdot \Delta V$, where I is the current, Δt is the discharge time, m is the electrode mass, and ΔV is the voltage window. As the scan rate increases, the specific capacitance tends to decrease, reflecting limited ion diffusion at higher rates [46]. **Figure 6(c)** shows the cycling stability of the electrode material, which

maintains excellent stability over 5,000 charge-discharge cycles at a current density of 1 $A \cdot g^{-1}$.

Further comparison of the rate of increase in potential difference and specific capacitance revealed that the WO_3/rGO/AC sample exhibited the highest electrode efficiency, followed by the WO_3/rGO nanocomposite. The pure rGO electrode demonstrated the lowest specific capacitance, confirming that the WO_3/rGO/AC electrode delivered the best performance. **Figures 6(c)** and **6(d)** show the results of a stability study conducted from cycle 100 to cycle 5,000. The results indicate that the WO_3/rGO/AC electrode is highly stable, as evidenced by a relatively small decrease in the voltammogram between cycle 1 and cycle 5,000. This confirms the excellent stability of the WO_3/rGO/AC electrode.

The charge-discharge performance of the WO_3/rGO/AC samples using a three-electrode system is shown in **Figure 6(e)**. Galvanostatic charge-discharge (GCD) measurements are a common and reliable method for evaluating electrochemical performance. The specific capacitance was calculated within a current range of 1 - 5 $A \cdot g^{-1}$. It was observed that as the current increased, the charging rate improved while the discharge time decreased, as shown in **Figure 7(a)**. When the equivalent series resistance (R_{ESR}) was calculated to be 50 Ω, the pure rGO and WO_3 electrodes exhibited lower Δt values compared to the WO_3/rGO nanocomposites.

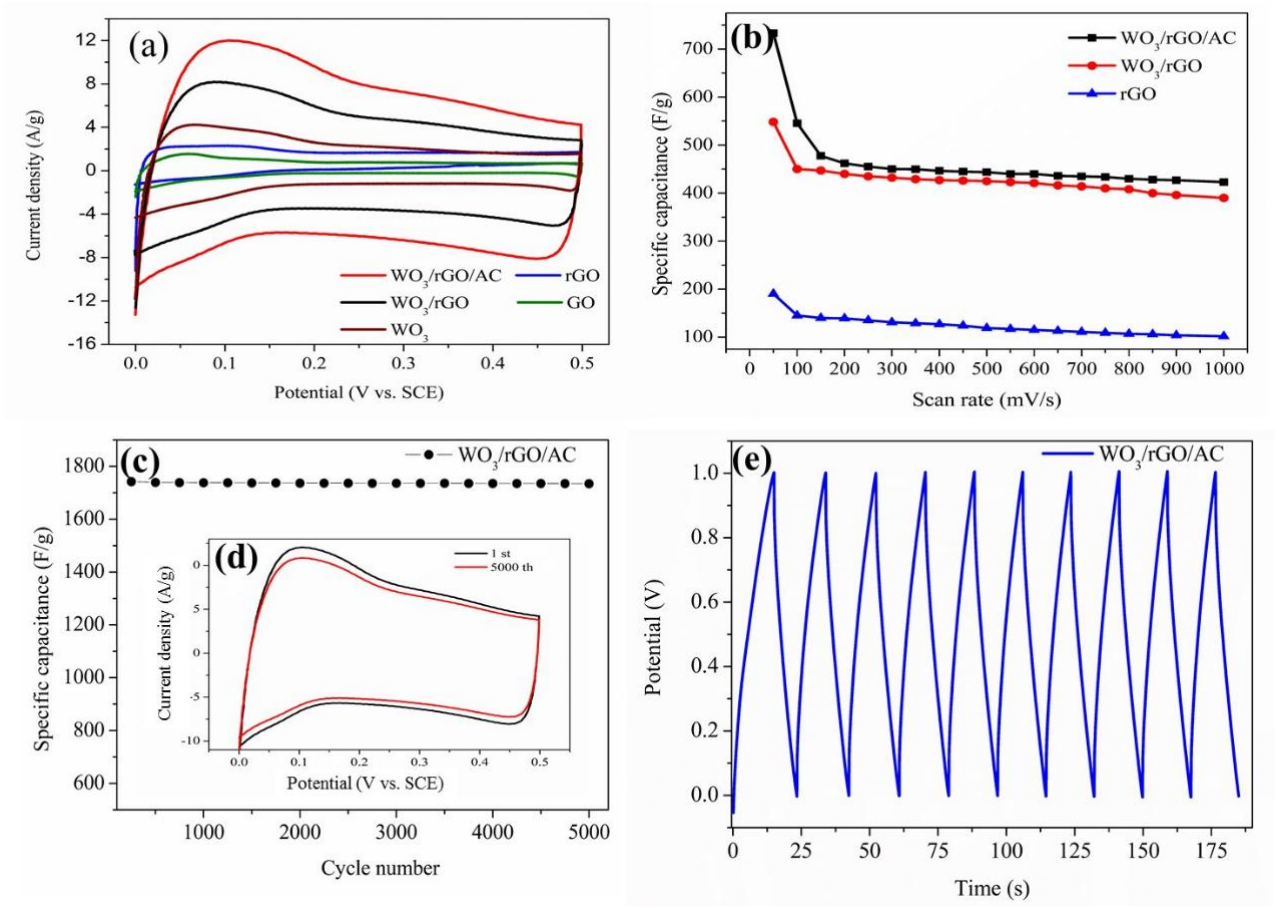

Figure 6 (a) Cyclic voltammetry data of GO, rGO, WO_3, WO_3/rGO and WO_3/rGO/AC composites with a potential range of 0 - 0.5 V, scan rate of 50 $mV \cdot s^{-1}$ in 2 M KOH, (b) Specific capacitance vs. scan rate of rGO, WO_3/rGO and WO_3/rGO/AC, (c) Stability from the 100th cycle to the 5,000th cycle; (d) Cyclic voltammogram of the sample for the 5,000th cycle; and (e) Galvanostatic charge-discharge (GCD) curves at 1 $A \cdot g^{-1}$ for 10 cycles.

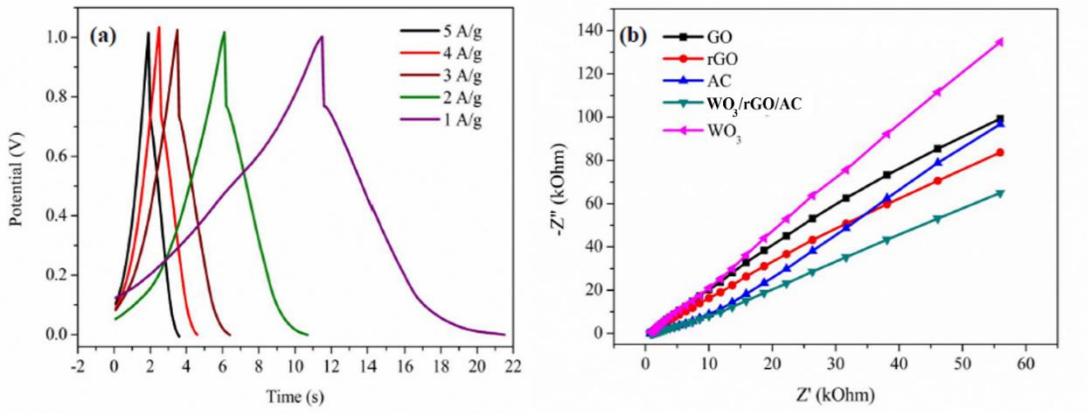

Figure 7 (a) Galvanostatic charge-discharge (GCD) curves at various current densities, (b) Electrochemical impedance spectroscopy (EIS) of GO, rGO, WO_3, AC, and WO_3/rGO/AC in 2 M KOH solution over a frequency range of 0.1 Hz - 100 kHz.

Figure 7 presents the electrochemical performance of various electrode materials through (a) galvanostatic charge-discharge (GCD) curves and (b) electrochemical impedance spectroscopy (EIS) plots. In **Figure 7(a)**, the GCD curves at different current densities (1-5 $A \cdot g^{-1}$) exhibit nearly triangular shapes, indicating capacitive behavior. As the current increases, the discharge time decreases due to higher internal resistance and lower charge storage capacity. The symmetrical curves reflect efficient charge storage and rapid charge transfer kinetics.

Figure 7(b) shows the electrochemical impedance spectroscopy (EIS) values of GO, rGO, WO_3, AC, and WO_3/rGO/AC samples in 2 M KOH solution over the frequency range of 0.1 Hz to 100 kHz, used to study and compare the complex resistivity properties in Nafion-117 solution. It was found that the complex resistivity of the WO_3 electrode is the highest, followed by GO, rGO, AC, and WO_3/rGO/AC, respectively, with the WO_3 electrode exhibiting the highest electrical insulating properties. The GO electrode has a lower resistance than the WO_3 electrode because it still contains some charge carriers that can conduct electricity, making its complex resistance lower than that of the WO_3 electrode.

When comparing the AC electrode with the rGO electrode, it was found that at low frequencies (complex resistance values lower than Z' < 20 kΩ), the AC electrode has a lower complex resistance value than rGO. However, at high frequencies (complex resistance values higher than Z′ > 20 kΩ), the AC electrode has a higher complex resistance value than rGO, indicating that the rGO electrode responds well at high frequencies. The electrochemical complex resistance (EIS) value reflects the ionic resistance of the electrolyte and the internal resistance between the electrode materials and current collector [47]. It also accounts for Faradaic reaction and charge transfer resistance in active materials (Rct). The C_{pe} represents the stationary phase component described by the pseudocapacitance, and (Z'') indicates the Warburg resistance due to ion diffusion on the electrode surface [48]. The steeper vertical line in the EIS plot for WO_3/rGO/AC > WO_3/rGO > AC > GO > WO_3 suggests excellent electron conductivity from the rGO layer [49]. Additionally, this corresponds to the maximum value of the imaginary part (Z'') and the time constant (τ), calculated from the frequency (f*) as shown in the equation below.

$$\tau = \frac{1}{2\pi f^*} \quad (1)$$

Table 1 presents the nitrogen adsorption-desorption results and calculated electrochemical performance metrics—including specific capacitance (Csp), energy density (E), and power density (P)—for 6 different composite materials: GH, GH (annealed), rGO, AC, WO_3/rGO, and WO_3/rGO/AC. The specific surface

areas, measured from nitrogen adsorption isotherms, were 13.90, 20.25, 645.67, 1,822.76, 102.89 and 834.12 $m^2 \cdot g^{-1}$, respectively. The corresponding specific capacitances were 28.33, 52.52, 117.22, 137.25, 697.29 and 733.30 $F \cdot g^{-1}$, respectively. Among them, GH exhibited the lowest surface area and capacitance. However, after calcination at 300 °C, the surface area of GH increased due to the thermal decomposition of impurities, which created a more porous structure and increased its capacitance.

The rGO sample showed a high specific surface area of 645.67 $m^2 \cdot g^{-1}$, consistent with previous reports. For example, rGO synthesized via the hydrothermal method can reach surface areas up to 1,435 $m^2 \cdot g^{-1}$ [49]. However, this value remains lower than the theoretical surface area of graphene (2,640 $m^2 \cdot g^{-1}$) [50] due to the presence of oxygen-containing functional groups on rGO, which limit its full exfoliation and surface accessibility.

The WO_3/rGO heterostructure, despite having a lower surface area (102.89 $m^2 \cdot g^{-1}$), achieved a very high capacitance (697.29 $F \cdot g^{-1}$), attributed to the pseudocapacitive behavior of WO_3 and its efficient interaction with the rGO support. The nitrogen adsorption isotherm indicated that rGO effectively supported the immobilization of WO_3 nanoparticles, preventing their agglomeration and thereby improving the electrochemical efficiency of the composite.

The WO_3/rGO/AC composite further enhanced performance by incorporating activated carbon, which contributed a large surface area (834.12 $m^2 \cdot g^{-1}$) and dual capacitive behavior (EDLC and pseudocapacitance). Although the surface area of WO_3/rGO is relatively low, its Faradaic contribution significantly boosts capacitance. The combination of WO_3/rGO and AC yielded the highest capacitance (733.30 $F \cdot g^{-1}$), highest energy density (101.85 $Wh \cdot kg^{-1}$), and highest power density (16,109.40 $W \cdot kg^{-1}$) in this study, demonstrating a strong synergistic effect.

Table 1 Calculation of specific capacity (Csp), energy density (E), and power (P) of different composite materials.

Type	Surface area ($m^2 \cdot g^{-1}$)	C_{sp} ($F \cdot g^{-1}$)	t (discharge: s)	E ($Wh \cdot kg^{-1}$)	P ($W \cdot kg^{-1}$)
GH	13.90	28.33	30.00	3.93	472.17
GH annealed	20.25	52.52	35.00	7.29	750.29
rGO	645.67	117.22	22.12	16.28	2,649.64
AC	1822.76	137.25	27.50	19.06	2,495.45
WO_3/rGO	102.89	697.29	36.60	96.85	9,525.82
WO_3/rGO/AC	834.12	733.30	22.76	101.85	16,109.40

Conclusions

In summary, this project successfully synthesized graphene oxide (GO), reduced graphene oxide (rGO), activated carbon (AC), tungsten oxide (WO_3), and WO_3/rGO nanocomposites using a microwave-assisted chemical process. The synthesized samples were characterized using various techniques to study their physical structure and electrochemical properties. Raman spectroscopy confirmed the presence of the desired chemical compounds, while X-ray diffraction (XRD) analysis indicated that the samples exhibited monoclinic crystal structures. Morphological analysis showed that the WO_3 nanoparticles had an average diameter of 21.56 ± 0.0834 nm. In the WO_3/rGO nanocomposites, rGO provided thermal stability, with WO_3 content measured at 17 wt%. Electrochemical testing using a screen-printed electrode setup showed that the WO_3/rGO/AC composite exhibited the highest specific capacitance of 733.30 $F \cdot g^{-1}$. When configured as a supercapacitor, it reached a peak capacitance of 1,742.16 $F \cdot g^{-1}$ at 250 cycles and demonstrated excellent stability over more than 5,000 cycles. The WO_3 nanoparticles and activated carbon significantly contributed to the enhanced charge storage capability. These results confirm that the developed synthesis method is both effective and economical, offering strong potential for future applications in energy storage systems, such as power banks.

To make this research more understandable, the project focused on creating a new material that can store electrical energy more efficiently-similar to how batteries or power banks work. We combined several substances, including forms of carbon (graphene oxide and activated carbon) and a metal oxide (tungsten oxide), using a quick and cost-effective heating method. The final product is a composite material that was tested and proven to be stable, efficient, and capable of storing a large amount of energy for a long time. Notably, adding activated carbon further improved its performance. This new material holds promise for improving the quality and lifespan of energy storage devices used in everyday electronics.

Acknowledgements

This study was funded by a research grant from Rajamangala University of Technology Rattanakosin, Thailand.

Declaration of Generative AI in Scientific Writing

Portions of the language in this manuscript were edited with the assistance of a generative AI language model (ChatGPT, developed by OpenAI). The authors have thoroughly reviewed and verified all AI-generated content to ensure accuracy and scientific validity.

CRediT Author Statement

Mr. Santi Rattanaveeranon conceptualized the study, designed and conducted the experiments, synthesized the materials, performed the characterization, analyzed the data, and drafted the manuscript. **Asst. Prof. Knavoot Jiamwattanapong** contributed to the interpretation of results, provided suggestions for manuscript improvement, and assisted with language editing.

References

[1] M Khan, MN Tahir, SF Adil, HU Khan, MRH Siddiqui, AA Al-warthan and W Treme. Graphene-based metal and metal oxide nanocomposites: Synthesis, properties, and their applications. *J. Mater. Chem. A* 2015; **3(37)**, 18753-18808.

[2] DC Marcano, DV Kosynkin, JM Berlin, A Sinitskii, Z Sun, A Slesarev, LB Alemany, W Lu and JM Tour. Improved synthesis of graphene oxide. *ACS Nano* 2010; **4(8)**, 4806-4814.

[3] J Wei, T Vo and F Inam. Epoxy/graphene nanocomposites-processing and properties: A review. *RSC Advances* 2015; **5(90)**, 73510-73524.

[4] SD Dabhi, SD Gupta and PK Jha. Structural, electronic, mechanical, and dynamical properties of graphene oxides: A first-principles study. *J. Appl. Phys.* 2014; **115(20)**, 203517.

[5] J Li, X Zeng, T Ren and EV der Heide. The preparation of graphene oxide and its derivatives and their application in bio-tribological systems. *Lubricants* 2014; **2(3)**, 137-161.

[6] S Pei and HM Cheng. The reduction of graphene oxide. *Carbon* 2012; **50(9)**, 3210-3228.

[7] MTH Aunkor, IM Mahbubul, R Saidurb and HSC Metselaar. The green reduction of graphene oxide. *RSC Advances* 2016; **6(33)**, 27807-27828.

[8] HJ Shin, KK Kim, A Benayad, SM Yoon, HK Park, IS Jung, MH Jin, HK Jeong, JM Kim, JY Choi and YH Lee. Efficient reduction of graphite oxide by sodium borohydride and its effect on electrical conductance. *Adv. Funct. Mater.* 2009; **19(12)**, 1987-1992.

[9] B Gurzęda, P Florczak, M Wiesner, M Kempinski, S Jurgabe and P Krawczyk. Graphene material prepared by thermal reduction of the electrochemically synthesized graphite oxide. *RSC Advances* 2016; **6(67)**, 63058-63063.

[10] D Voiry, J Yang, J Kupferberg, R Fullon, C Lee, HY Jeong, HS Shin and M Chhowalla. High-quality graphene via microwave reduction of solution-exfoliated graphene oxide. *Science* 2016; **353(6306)**, 1413-1416.

[11] H Yoo, Y Kim, J Lee, H Lee, Y Yoon, G Kim and H Lee. n-Type reduced graphene oxide field-effect transistors (FETs) from photoactive metal oxides. *Chem. Euro. J*. 2012; **18(16)**, 4923-4929.

[12] RYN Gengler, DS Badali, D Zhang, K Dimos, K Spyrou, D Gournis and RJD Miller. Revealing the ultrafast process behind the photoreduction of graphene oxide. *Nature Communications* 2013; **4**, 2560.

[13] M Toselli, D Fabiani, P Mancinelli, M Frechette, T Heid, E David and A Saccani. In situ thermal reduction of graphene oxide forming epoxy nanocomposites and their dielectric properties.

Polymer Composites 2015; **36(2)**, 294-301.

[14] S Wu, Q Jia and W Dai. Synthesis of RGO/TiO_2 hybrid as a high-performance photocatalyst. *Ceram. Int.* 2017; **43(1)**, 1530-1535.

[15] Y Wang, H Guan, C Dong, X Xiao, S Du and Y Wang. Reduced graphene oxide (RGO)/Mn_3O_4 nanocomposites for dielectric loss properties and electromagnetic interference shielding effectiveness at high frequency. *Ceram. Int.* 2016; **42(1)**, 936-942.

[16] K Anand, O Singh, MP Singh, J Kaur and RC Singh. Hydrogen sensor based on graphene/ZnO nanocomposite. *Sens. Actuators B Chem.* 2014; **195**, 409-415.

[17] S Kumar, AK Ojha and B Walkenfort. Cadmium oxide nanoparticles grown in situ on reduced graphene oxide for enhanced photocatalytic degradation of methylene blue dye under ultraviolet irradiation. *J. Photochem. Photobiol. B* 2016; **159**, 111-119.

[18] L Khandare and DJ Late. MoO_3-rGO nanocomposites for electrochemical energy storage. *Appl. Surf. Sci.* 2017; **418**, 2-8.

[19] Z Ji, X Shen, M Li, H Zhou, G Zhu and K Chen. Synthesis of reduced graphene oxide/CeO_2 nanocomposites and their photocatalytic properties. *Nanotechnology* 2013; **24(11)**, 115603.

[20] Y Yang, ZA Hu, ZY Zhang, FH Zhang, YJ Zhang, PJ Liang, HY Zhang and HY Wu. Reduced graphene oxide-nickel oxide composites with high electrochemical capacitive performance. *Mater. Chem. Phys.* 2012; **133(1)**, 363-368.

[21] C Xiang, M Li, M Zhi, A Manivannan and N Wu. A reduced graphene oxide/Co_3O_4 composite for supercapacitor electrode. *J. Power Sources* 2013; **226**, 65-70.

[22] R Bhargava and S Khan. Superior dielectric properties and bandgap modulation in hydrothermally grown Gr/MgO nanocomposite. *Phys. Lett. A* 2019; **383(14)**, 1671-1676.

[23] D Sanchez-Martinez, AMDL Cruz and E Lopez-Cuellar. Synthesis of WO_3 nanoparticles by citric acid-assisted precipitation and evaluation of their photocatalytic properties. *Mater. Res. Bull.* 2013; **48(2)**, 691-697.

[24] Q Xiang, GF Meng, HB Zhao, Y Zhang, H Li, WJ Ma and JQ Xu. Au nanoparticle modified WO_3 nanorods with their enhanced properties for photocatalysis and gas sensing. *J. Phys. Chem.* 2010; **114(5)**, 2049-2055.

[25] L Santos, CM Silveira, E Elangovan, JP Neto, D Nunes, L Pereira, R Martins, J Viegas, JJG Moura, S Todorovic, MG Almeida and E Fortunato. Synthesis of WO_3 nanoparticles for biosensing applications. *Sens. Actuators B Chem.* 2016; **223**, 186-194.

[26] D Shao, M Yu, J Lian and S Sawyer. Ultraviolet photodetector fabricated from 3D WO_3 nanowires/reduced graphene oxide composite material. *MRS Proc.* 2014; **1659**, 193-198.

[27] D Mao, S Zhang, Y Wang, X Gan, W Zhang, T Mei, Y Wang, Y Wang, H Zeng and J Zhao. WS_2 saturable absorber for dissipative soliton mode locking at 1.06 and 1.55 μm. *Opt. Express* 2015; **23(21)**, 27509-27519.

[28] J Chu, D Lu, X Wang, X Wang and S Xiong. WO_3 nanoflower coated with graphene nanosheet: Synergetic energy storage composite electrode for supercapacitor application. *J. Alloys Compd*. 2017; **702(1)**, 568-572.

[29] DR Dreyer, S Park, CW Bielawski and RS Ruoff. The chemistry of graphene oxide. *Chem. Soc. Rev.* 2010; **39**, 228-240.

[30] S Rattanaveeranon, K Jiamwattanapong and N Jandee. Effect of durian peel ash added in zinc oxide/reduced graphene oxide composites used as a chemical sensor for hydrazine detection. *Mater. Sci. Appl.* 2021; **12(2)**, 111-120.

[31] S Hilaire, MJ Suess, N Kranzlin, K Bienkowski, R Solarska, J Augustynski and M Niederberger. Microwave-assisted nonaqueous synthesis of WO_3 nanoparticles for crystallographically oriented photoanodes for water splitting. *J. Mater. Chem. A* 2014; **2(48)**, 20530-20537.

[32] BS Rodrigues, M Niederberger and JS Souza. Exploring the effects of synthesis parameters on the properties and photoactivity of WO_3-graphene oxide synthesized via a microwave route. *Mater. Adv.* 2024; **5(11)**, 4889-4901.

[33] S Rattanaveeranon, K Jiamwattanapong and R Suntako. Enhancement of specific capacitance using a mixture of sweet potato ash and zinc oxide

nanoparticles on reduced graphene oxide sheets. *Russ. J. Appl. Chem.* 2024; **97(11)**, 827-836.

[34] R Bhargava and S Khan. Superior dielectric properties and bandgap modulation in hydrothermally grown Gr/MgO nanocomposite. *J. Mater. Sci.* 2021; **56(5)**, 1671–1676.

[35] H Yang, F Li, C Shan, D Han, Q Zhang, L Niu and A Ivaska. Covalent functionalization of chemically converted graphene sheets *viasilane* and its reinforcement. *J. Mater. Chem.* 2009; **19(26)**, 4632-4638.

[36] Q Zheng, G Fang, F Cheng, H Lei, W Wang, P Qin and H Zhou. Hybrid graphene-ZnO nanocomposites as electron acceptor in polymer-based bulk-heterojunction organic photovoltaics. *J. Phys. D: Appl. Phys.* 2012; **45(45)**, 455103.

[37] B Ma, E Huang, G Wu, W Dai, N Guan and L Li. Fabrication of $WO_{2.72}$/RGO nano-composites for enhanced photocatalysis. *RSC Advances* 2017; **7(5)**, 2606-2614.

[38] N Huo, S Yang, Z Wei and J Li. Synthesis of WO_3 nanostructures and their ultraviolet photoresponse properties. *J. Mater. Chem. C* 2013; **1(25)**, 3999-4007.

[39] Y Gu, Q Zhuo and D Wu. Large-mesopore hierarchical tungsten trioxide hydrate with exposed high-energy facets: Facile synthesis and enhanced photocatalysis. *Mater. Sci. Semicond. Process.* 2016; **53**, 18-27.

[40] N Ahmad, S Khan, MMN Ansari and R Bhargava. A comprehensive study of structural and electrical properties of SnO_2 and $Sn_{0.95}Mn_{0.05}O_2$. *AIP Conf. Proc.* 2018, **1942(1)**, 050007.

[41] M Huang, Y Wu and W Hu. A facile synthesis of reduced graphene oxide-wrapped WO_3 nanowire composite and its enhanced electrochemical catalysis properties. *Ceram. Int.* 2014; **40(5)**, 7219-7225.

[42] X An, CY Jimmy, Y Wang, Y Hu, X Yu and G Zhang. WO_3 nanorods-graphene nanocomposites for high-efficiency visible-light-driven photocatalysis and NO_2 gas sensing. *J. Mater. Chem.* 2012; **22(17)**, 8525-8531.

[43] BE Turkaslan, AK Çelik, A Dalbeyler and N Fantuzzi. The effect of different morphologies of WO_3/GO nanocomposite on photocatalytic performance. *Materials* 2022; **15(22)**, 8019.

[44] P Nagaraju, A Alsalme, AM Alkathiri and R Jayavel. Rapid synthesis of WO_3-graphene nanocomposite via in-situ microwave method with improved electrochemical properties. *J. Phys. Chem. Solids* 2018; **120**, 250-260.

[45] A Baserga, V Russo, FD Fonzo, A Bailini, D Cattaneo, CS Casari, A Li Bassi and CE Bottani. Nanostructured tungsten oxide with controlled properties: Synthesis and Raman characterization. *Thin Solid Films* 2007; **515(16)**, 6465-6469

[46] SH Mujawar, SB Ambade, T Battumur, RB Ambade and SH Lee. Electropolymerization of polyaniline on titanium oxide nanotubes for supercapacitor application. *Electrochim. Acta* 2011; **56(12)**, 4462-4466.

[47] Y Yang, Y Liang, Y Zhang, Z Zhang, Z Li and Z Hu. Three-dimensional graphene hydrogel supported ultrafine RuO_2 nanoparticles for supercapacitor electrodes. *New J. Chem.* 2015; **39(5)**, 4035-4040.

[48] M Rethinasabapathy, SM Kang, SC Jang and YS Huh. Three-dimensional porous graphene materials for environmental applications. *Carbon Lett.* 2017; **22(1)**, 1-13.

[49] CPP Wong, CW Lai, KM Lee, JC Juan and SBA Hamid. Synthesis of reduced graphene oxide/tungsten trioxide nanocomposite electrode for high electrochemical performance. *Ceram. Int.* 2016; **42(11)**, 13128-13135.

[50] AR Ravindran, C Feng, S Huang, Y Wang, Z Zhao and J Yang. Effects of graphene nanoplatelet size and surface area on the AC electrical conductivity and dielectric constant of epoxy nanocomposites. *Polymers* 2018; **10(5)**, 477.